Paper for Electrochemistry Communications. *10 March 2017*

3D-printed porous electrodes for advanced electrochemical flow reactors: A Ni/stainless steel electrode and its mass transport characteristics

L.F. Arenas, C. Ponce de León*, F.C. Walsh

Electrochemical Engineering Laboratory, Energy Technology Group,

Faculty of Engineering and the Environment, University of Southampton SO17 1BJ, UK.

* Author for correspondence: capla@soton.ac.uk

ABSTRACT

Porous electrodes have shown high performance in industrial electrochemical processes and redox flow batteries for energy storage. They offer great advantages over planar electrodes in terms of higher space time yield and enhanced mass transport. In this work, a highly ordered porous stainless steel electrode was manufactured by 3D-printing and coated with nickel from an acidic bath by electrodeposition in a divided rectangular channel flow cell. Following electrodeposition, the volumetric mass transport coefficient of this electrode was determined by the electrochemical reduction of 1.0×10^{-3} mol dm^{-3} of ferricyanide ions by linear sweep voltammetry and chronoamperometry. The convection diffusion characteristics are compared with other geometries to demonstrate the novelty and the advantages of 3D-printed porous electrodes in electrochemical flow reactors. Robust porous electrodes with tailored surface areas, volumetric porosity and flow properties are possible.

Keywords: additive manufacturing, 3D-printing, electrochemical engineering, electrochemical flow reactor, mass transport, porous electrode

Corresponding author: C. Ponce de León: capla@soton.ac.uk

1. Introduction

In this contribution, we present a novel 3D-printed flow reactor electrode with a complex, intricate geometry which cannot be realised by computer numerical control (CNC) machining or other classical manufacturing methods. Such 3D-printed electrodes offer an alternative to the currently available metal and carbon-based meshes, foams and felts, delivering a new genre of free-form porous electrodes having tailored composition, catalytic activity, active surface area, fluid flow characteristics and mass transport properties. Porous electrodes in flow-by configuration offer a substantial increase in active surface area, mass transport and space time yield in comparison to planar electrodes [1]. Their industrial applications include inorganic and organic electrosynthesis (including pharmaceutics), treatment of process streams, metal recovery and electrolysis reactions [2].

Although additive manufacturing (3D-printing) has been available for over 30 years [3], there are few examples of electrochemical devices using this constantly evolving technology. In previous work, we applied 3D-printing as a fast prototyping tool for the development of the polymer bodies of laboratory flow reactors and redox flow batteries [4]. However, it is more desirable to 3D-print the interface at which the electrode process takes place. Interest in 3D-printed electrochemical devices is growing [5], but has been largely restricted to microfluidics, capacitors and sensors, for instance, interdigitated supercapacitors [6], micro-supercapacitors [7] and micro-electrochemical cells. Other recent work involves serpentine flow field plates for cells with gaseous streams such as H_2/O_2 [8] and methanol [9,10] micro-fuel cells, and a miniature Ag/propylene PEM electrolyser [11]. In flow reactors with liquid electrolytes, only fast prototyping of electrolyte flow channels and manifolds has been performed [4,12,13]. These studies show that the performance of electrochemical cells and electrodes employing additive manufacturing in their construction can be higher than those manufactured by

conventional methods. 3D-printing offers low-cost, flexibility of materials and rapid turnover prototypes to aid the optimisation of specific applications.

The concept of 3D-printed electrodes for electrochemical flow reactors is demonstrated here by determining the mass transport characteristics of a 3D-printed porous, nickel-coated stainless steel (Ni/SS) cathode with a projected area of 24 cm^2 in the flow-by configuration from the limiting current for ferricyanide ion reduction:

$$[Fe(CN)_6]^{3-} + e^- \rightarrow [Fe(CN)_6]^{4-} \quad (1)$$

over a range of controlled mean linear flow velocity of electrolyte. Under full convective-diffusion reaction control, the volumetric mass transport coefficient, $k_m A_e$, is the product of mass transport coefficient, k_m and active electrode area per unit volume, A_e. It is related to the limiting current, I_L, concentration, c, and number of electrons, z, by:

$$k_m A_e = \frac{I_L}{zFcV_e} \quad (2)$$

where F is Faraday's constant and V_e is the total volume of the electrode within the flow cell. This is one of the main performance factors used to estimate the required size of an electrochemical reactor for a given conversion rate [2]. One of the principal advantages for 3D-printed electrodes is the possibility of controlling the term A_e in equation (2) by producing a desired geometry, enabling electrode materials with tailored $k_m A_e$. Furthermore, k_m depends on the electrode geometry, orientation, volumetric porosity and surface roughness, which can also be controlled to a certain degree in 3D-printed materials. For instance,

geometrically complex hierarchical porous structures with new properties can be produced with high-resolution 3D-printing [14].

2. Experimental details

2.1 Manufacture of the 3D-printed stainless steel electrodes

The stainless steel porous electrode consists of a 60.0 × 40.0 × 3.7 mm rectangular parallelepiped broken through by a hexagonal grid of tiled empty spherical volumes, each of 1.8 mm diameter, forming a continuous body with a 68.0 × 45.0 × 2.0 mm stainless steel plate current collector. The centres of the spheres were separated from each other by a distance of 1.7 mm so that the void volumes would intersect. The cross-sectional area, A_X, of the porous matrix was 1.48 cm^2 and its volumetric porosity, ε, was 63.9%, as measured by liquid volume displacement. The electrode was designed using Meshmixer (Autodesk Inc.) software and manufactured in M2 Multilaser (Concept Laser GmbH) additive manufacturing equipment with CL 20ES stainless-steel powder 316L containing approx. 17% Cr, 13% Ni, 2% Mo, the balance being Fe. The powder particles are approx. 20-40 μm diameter and the electrode is formed layer-by-layer through a re-coater, applying 200 W laser (near-IR 1070 nm) to melt the material under an N_2 atmosphere. A custom-built positioning system was used to translate computer-aided design structures into the printed object.

2.2 Electrodeposition of nickel on the stainless steel electrode

The nickel coating was applied with the purpose of avoiding the passivation of stainless steel during the limiting current experiments in an aqueous Na_2CO_3 electrolyte [15]. The experimental arrangement used to deposit nickel on the 3D-printed stainless steel was similar to that described in [16]. The components and dimensions of the flow cell are given in a previous work [17]. The porous stainless steel electrode occupied the negative flow channel while inert polypropylene ‘turbulence promoters’ maintained a constant separation between

the membrane and the Pt/Ti plate electrode in the positive flow channel. Hydraulic sealing was achieved with mechanical compression and silicone rubber gaskets. Masterflex L/S (Cole-Parmer Co) peristaltic pumps were used to circulate the electroplating solutions in the negative half-cell and the supporting electrolyte in the positive half-cell.

The nickel coating was applied galvanostatically with an EX752M power supply (TT Instruments Ltd) according to a procedure described in [18]. Nickel was deposited at 100 mA cm^{-2} (based on the projected electrode area) for 60 s in a 'Wood's strike' bath and then for 240 s in a Watt's bath at the same current density. The electrode was pre-treated with 50% w/v HCl for 180 s, rinsed with deionised water, then with 40% w/v NaOH for 300 s, cathodically cleaned at 15 mA cm^{-2} for 60 s in the same solution and rinsed.

2.3 Mass transport studies on the nickel-coated 3D-printed electrode

Fig. 1 shows the experimental set up used for the mass transport studies. A three-electrode cell configuration was implemented, with the 3D-printed working electrode (WE), a Pt/Ti plate counter-electrode (CE) and a Hg/Hg_2SO_4 (sat.) reference electrode (RE) connected via a Luggin capillary. The cell was controlled with an Autolab potentiostat (Metrohm AG). A Nafion® (DuPont Co) 112 cation exchange membrane was used as separator. The electrolyte composition is: 1.0×10^{-3} mol dm^{-3} of $K_3[Fe(CN)_6]$, 10.0×10^{-3} mol dm^{-3} of $K_4[Fe(CN)_6]$, 1.0 mol dm^{-3} of Na_2CO_3. Limiting current measurements for ferricyanide ion reduction were conducted by linear sweep voltammetry between 0.2 V and −0.6 V *vs*. Hg/Hg_2SO_4 at a linear potential sweep rate of 5 mV s^{-1} and by chronoamperometry at a constant potential of −0.5 V *vs.* Hg/Hg_2SO_4. Volumetric flow rates between 50 and 350 cm^3 min^{-1} were evaluated, equivalent to mean linear flow velocities, ($v = Q_v/\varepsilon A_X$) between 0.88 and 6.17 cm s^{-1} with the aid of peristaltic pumps. A temperature of 25 ^{o}C was maintained with a thermostatic bath.

3. Results and discussion

3.1 Electrode structure

The regular, 3D-printed macroporous structure of the flow-by electrode and attached current collector can be appreciated in Fig. 2a). Controlled manufacturing conditions avoided significant thermal deformation or any internal porosity resulting in undesired hydraulic permeability. Fig. 2b) shows an optical microscopy image of the electrode side view at the entrance of the flow channel. The electrode and the current collector/feeder form a single continuous metallic electrode. An advantage of this configuration, made possible by 3D-printing, is that it eliminates corrosion or passivation susceptibility at this interphase together with the need to use mechanical compression, conductive adhesives or welding to ensure reliable transfer of the current from the porous matrix to the planar current collector. In electrochemical reactors and redox flow batteries, such interphase can have a relatively high electrical resistivity, varying with compression force (e.g. in [19]) or number of welding points, with their associated non-uniform current distribution.

Fig. 2b) also reveals a high degree of surface roughness, local heterogeneity and surface micro-porosity at the electrode structure as a result of the additive manufacturing process involving laser melting of metal powder. This roughness increases the surface area of the electrode and creates micro turbulence that enhances mass transport [20]. An SEM image of an opening in the front section of the electrode is shown in Fig. 2c). Nodular structures <100 μm in diameter generated by the laser melting are observed. Fig. 2d) presents a nickel EDS map for the same pore, confirming the electrodeposition of this metal in this region of the electrode.

3.2 Electrochemical performance

Fig. 3a) shows a series of typical polarisation curves for the reduction of 1.0×10^{-3} mol dm^{-3} of $[Fe(CN)_6]^{3-}$ at a linear potential sweep rates of 5 mV s^{-1}. The curves show the characteristic

limiting current plateau that stretches from −0.35 V to −0.6 V *vs*. Hg/Hg_2SO_4. By increasing the mean linear flow rate from 0.88 cm s^{-1} to 6.17 cm s^{-1}, the current at the 3D-printed electrode varies from 18 to 38 mA. The exploratory polarisation curves permitted to select a potential of –0.5 V in order to perform chronoamperometry under steady state convective-diffusion control. Triplicate current *vs*. time responses were recorded in these conditions, one of them is shown in Fig. 3b). Limiting current steps are observed resulting from increasing steps of electrolyte mean linear velocity performed at intervals of 30 s. As shown in Fig. 3c), the limiting currents obtained with the two methods are similar, here expressed as a current density calculated from the projected area of the electrode. The maximum percent error in the values determined by chronoamperometry was ±0.96%. In both cases, the background current was subtracted. Reproducible limiting currents at 3D-printed electrodes depend on the exact replication of the electrode geometry, surface roughness and electrocatalytic activity, in addition to maintaining reliable steady state and mass transport (related to flow rate).

The log-log plot in Fig. 3d) shows the relationship between $k_m A_e$ *vs*. mean linear flow velocity of the 3D-printed Ni/SS electrode along that of different available materials used as porous electrodes [21]. The values of $k_m A_e$ afforded by this 3D-printed electrode ranged from 2.03×10^{-2} s^{-1} to 5.05×10^{-2} s^{-1} at mean linear flow rates between 0.88 cm s^{-1} and 6.17 cm s^{-1}, being superior to perforated plates and typical expanded metal mesh, and comparable to reticulated vitreous carbon (RVC) 60 pores per inch (ppi). Electrodes with high surface area, such as carbon felt, nickel foam and wire wool (or felt) have higher $k_m A_e$ values, but different 3D-printed geometries with higher surface area, smaller pore size and higher roughness could easily be produced to approach those values. As the resolution of additive manufacturing improves [3], it might be possible to produce ordered matrixes made up by filaments approaching the fibre diameter of felts, as long as is economically viable for a specific application. Ti felt can have an average diameter close to 40 μm [17].

3.3 Perspective

Multi-material additive manufacturing is undergoing rapid progress [22] and complex porous structures can be routinely produced [14]. Meanwhile, the incorporation of catalysts in 3D-printed materials have shown promise in chemical reactors [23]. Such advances could be exploited in novel, composite or coated porous electrodes with enhanced mechanical and catalytic properties. Moreover, the geometry of 3D-printed electrodes could be devised to control current distribution, while bipolar electrodes for stacks could be easily manufactured.

This technology can also provide a deepened understanding of the relationship between porous geometries and mass transport through the validation of fluid flow models, taking a similar approach to [24]. Empirical and comparative studies of the pressure drop can also be performed, as this is usually considered in the characterization of flow reactors, *e.g.*, in [25]. Magnetic resonance imaging (MRI) [26] and X-ray computed tomography (CT) [16,27] are suitable techniques to characterize the structure and composition of porous electrodes and might be useful to determine their geometrical surface area, provided sufficiently small voxel size and high resolution.

The fabrication of entire, integrated electrochemical flow cells and stacks in a single operation is becoming possible [4]. In addition to 3D-printed electrodes, polymer flow cell bodies [12] and membranes [28] have already been realised. The demonstration of this technology could lead to innovative applications in several fields, such as electrochemical microfluidics and sensors [29] and small-scale electrosynthesis [30].

4. Conclusions

The mass transport characteristics of a Ni/SS 3D-printed porous electrode compare well and exceed those observed in typical planar, mesh and RVC electrodes. This opens the possibility to employ geometrically complex structures produced by additive manufacturing techniques as high performing, robust electrodes in specialised electrochemical flow reactors. Versatile, free-form electrodes can be tailored to achieve a specific electrode performance by controlling their active surface area and mass transport properties. Electrodes having different roughness, microstructure, orientation, composition, electrocatalysis and fluid flow environment can be 3D-printed.

Acknowledgements

LFA acknowledges the support provided by the Mexican government through CONACYT and SEP scholarships. All data supporting this study are openly available from the University of Southampton repository at http://doi.org/10.5258/SOTON/D0048.

References

[1] F.C. Walsh, L.F. Arenas, C. Ponce de León, G.W. Reade, I. Whyte, B.G. Mellor, The continued development of reticulated vitreous carbon as a versatile electrode material: Structure, properties and applications, Electrochim. Acta. 215 (2016) 566–591.

[2] D. Pletcher, F.C. Walsh, Industrial Electrochemistry, 2nd ed., Chapman and Hall, London, 1990.

[3] D.D. Gu, W. Meiners, K. Wissenbach, R. Poprawe, Laser additive manufacturing of metallic components: materials, processes and mechanisms, Int. Mater. Rev. 57 (2012) 133–164.

[4] L.F. Arenas, F.C. Walsh, C. Ponce de León, 3D-printing of redox flow batteries for energy storage: A rapid prototype laboratory cell, ECS J. Solid State Sci. Technol. 4 (2015) P3080–P3085.

[5] A. Ambrosi, M. Pumera, 3D-printing technologies for electrochemical applications, Chem. Soc. Rev. 45 (2016) 2740–2755. doi:10.1039/C5CS00714C.

[6] C. Zhao, C. Wang, R. Gorkin III, S. Beirne, K. Shu, G.G. Wallace, Three dimensional (3D) printed electrodes for interdigitated supercapacitors, Electrochem.

Commun. 41 (2014) 20–23.
[7] G. Sun, J. An, C.K. Chua, H. Pang, J. Zhang, P. Chen, Layer-by-layer printing of laminated graphene-based interdigitated microelectrodes for flexible planar micro-supercapacitors, Electrochem. Commun. 51 (2015) 33–36.
[8] G. Scotti, V. Matilainen, P. Kanninen, H. Piili, A. Salminen, T. Kallio, F. Sami, Laser additive manufacturing of stainless steel micro fuel cells, J. Power Sources. 272 (2014) 356–361.
[9] K. Alayavalli, D.L. Bourell, Fabrication of modified graphite bipolar plates by indirect selective laser sintering (SLS) for direct methanol fuel cells, Rapid Prototyping J. 16 (2010) 268–274.
[10] J. Weber, A.J. Wain, H. Piili, V.P. Matilainen, A. Vuorema, G.A. Attard, F. Marken, Residual porosity of 3D-LAM-printed stainless-steel electrodes allows galvanic exchange platinisation, ChemElectroChem. 3 (2016) 1020–1025.
[11] G. Chisholm, P.J. Kitson, N.D. Kirkaldy, L.G. Bloor, L. Cronin, 3D printed flow plates for the electrolysis of water: an economic and adaptable approach to device manufacture, Energy Environ. Sci. 7 (2014) 3026–3032. doi:10.1039/C4EE01426J.
[12] C. Ponce de León, W. Hussey, F. Frazao, D. Jones, E. Ruggeri, S. Tzortzatos, R.D. Mckerracher, R.G.A. Wills, S. Yang, F.C. Walsh, The 3D printing of a polymeric electrochemical cell body and its characterisation, Chem. Eng. Trans. 41 (2014) 1–6.
[13] H.A. Figueredo-Rodríguez, R.D. Mckerracher, C. Ponce de León, F.C. Walsh, Current distribution in a rectangular flow channel manufactured by 3D-printing, AIChE J. 63 (2016) 1144-1151.
[14] X. Zheng, W. Smith, J. Jackson, B. Moran, H. Cui, D. Chen, J. Ye, N. Fang, N. Rodriguez, T. Weisgraber, C. M. Spadaccini, Multiscale metallic metamaterials, Nature Materials. 15 (2016) 1100–1106.
[15] W.M. Taama, R.E. Plimley, K. Scott, Influence of supporting electrolyte on ferricyanide reduction at a rotating disc electrode, Electrochim. Acta. 41 (1996) 549–551.
[16] L.F. Arenas, C. Ponce de León, R.P. Boardman, F.C. Walsh, Electrodeposition of platinum on titanium felt in a rectangular channel flow cell, J. Electrochem. Soc. 164 (2017) D57–D66.
[17] L.F. Arenas, C. Ponce de León, F.C. Walsh, Mass transport and active area of porous Pt/Ti electrodes for the Zn-Ce redox flow battery determined from limiting current measurements, Electrochim. Acta. 221 (2016) 154–166.
[18] G.A. Di Bari, Electrodeposition of Ni, in: Modern Electroplating, M. Schlesinger, M. Paunovic (Eds.), 2010: pp. 79–114.
[19] E.A. Cho, U.S. Jeon, S.A. Hong, I.H. Oh, S.G. Kang, Performance of a 1kW-class PEMFC stack using TiN-coated 316 stainless steel bipolar plates, J. Power Sources.

142 (2005) 177–183.
[20] F.J. Recio, P. Herrasti, L. Vázquez, C. Ponce de León, F.C. Walsh, Mass transfer to a nanostructured nickel electrodeposit of high surface area in a rectangular flow channel, Electrochim. Acta. 90 (2013) 507–513.
[21] F.C. Walsh, A First Course in Electrochemical Engineering, The Electrochemical Consultancy, Romsey, 1993.
[22] M. Vaezi, S. Chianrabutra, B. Mellor, S. Yang, Multiple material additive manufacturing – Part 1: A review, Virtual Phys. Prototyp. 8 (2013) 19–50.
[23] M.D. Symes, P.J. Kitson, J. Yan, C.J. Richmond, G.J.T. Cooper, R.W. Bowman, T. Vilbrandt, L. Cronin, Integrated 3D-printed reactionware for chemical synthesis and analysis, Nature Chemistry. 4 (2012) 349–354.
[24] A. Inayat, J. Schwerdtfeger, H. Freund, C. Körner, R.F. Singer, W. Schwieger, Periodic open-cell foams: Pressure drop measurements and modeling of an ideal tetrakaidecahedra packing, Chem. Eng. Sci. 66 (2011) 2758–2763.
[25] C.J. Brown, F.C. Walsh, D. Pletcher, Mass transfer and pressure drop in a laboratory filterpress electrolyser, Trans. IChemE. 73 (1995) 196–205.
[26] G. Incera Garrido, F.C. Patcas, S. Lang, B. Kraushaar-Czarnetzki, Mass transfer and pressure drop in ceramic foams: A description for different pore sizes and porosities, Chem. Eng. Sci. 63 (2008) 5202–5217.
[27] E. Maire, X-ray tomography applied to the characterization of highly porous materials, Annu. Rev. Mater. Res. 42 (2012) 163–178.
[28] T. Femmer, A.J.C. Kuehne, M. Wessling, Print your own membrane: direct rapid prototyping of polydimethylsiloxane, Lab on a Chip. 14 (2014) 2610–2613.
[29] D.G. Rackus, M.H. Shamsi, A.R. Wheeler, Electrochemistry, biosensors and microfluidics: A convergence of fields, Chem. Soc. Rev. 44 (2015) 5320–5340.
[30] R.A. Green, R.C.D. Brown, D. Pletcher, B. Harji, A microflow electrolysis cell for laboratory synthesis on the multigram scale, Org. Process Res. Dev. 19 (2015) 1424–1427.

Figure captions

Fig. 1 Experimental arrangement for the mass transport studies of the 3D-printed Ni/SS porous electrode in a rectangular channel flow cell. The parallel plate electrodes are placed in flow-by configuration.

Fig. 2 3D-printed Ni/SS porous electrode. a) optical photography of the macro structure of the porous electrode, b) optical microscopy of the electrode (side view) and the integral current feeder, c) SEM of the micro structure of an individual pore opening (front view), d) nickel EDS mapping for the same pore opening.

Fig. 3 Mass transport studies of the 3D-printed Ni/SS porous electrode. a) Typical polarisation curves for the reduction of 1×10^{-3} mol dm^{-3} $K_4Fe(CN)_6$ in 1 mol dm^{-3} Na_2CO_3 at 25 ^{o}C. b) Chronoamperometry showing limiting currents at steps of increasing electrolyte mean linear flow rate. c) Comparison of the limiting current density obtained by linear sweep voltammetry and chronoamperometry. d) Volumetric mass transfer coefficient *vs*. mean linear flow velocity of the 3D-printed Ni/SS electrode against various porous electrode structures. Comparative data taken from [21].

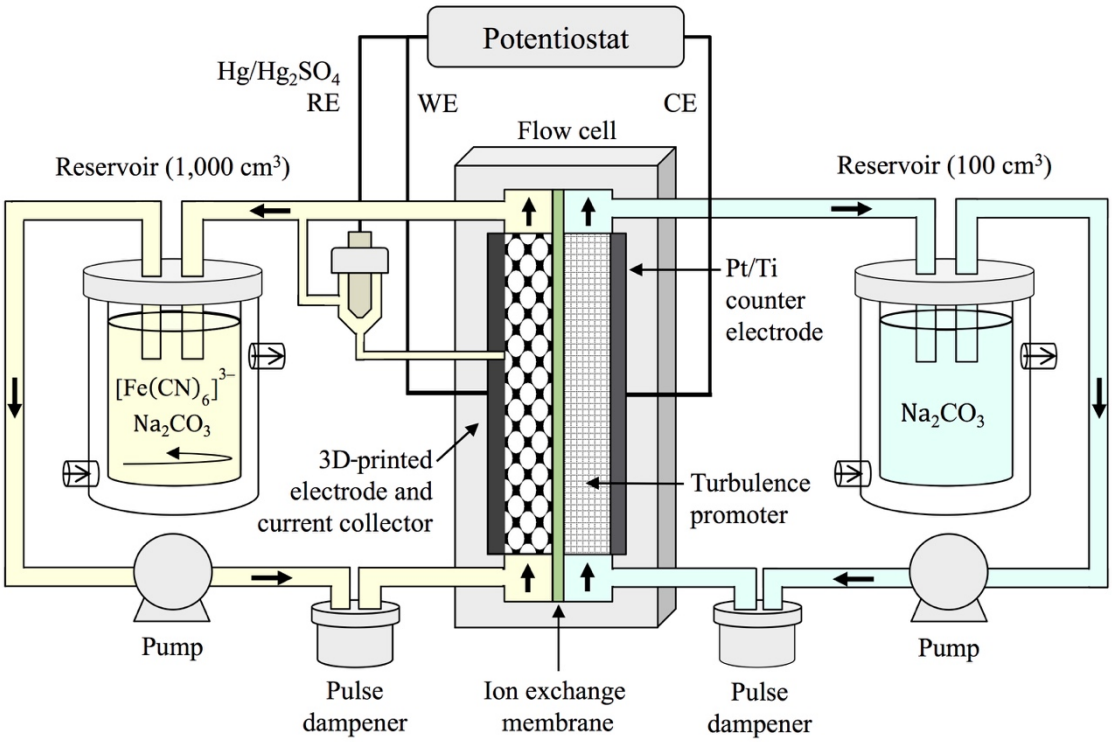
Potentiostat
Hg/Hg2SO4
RE
WE
CE
Flow cell
Reservoir (1,000 cm3)
Reservoir (100 cm3)
Pt/Ti
counter
electrode
[Fe(CN)6]3–
Na2CO3
Na2CO3
3D-printed
electrode and
current collector
Turbulence
promoter
Pump
Pump
Pulse
dampener
Ion exchange
membrane
Pulse
dampener

Fig. 1

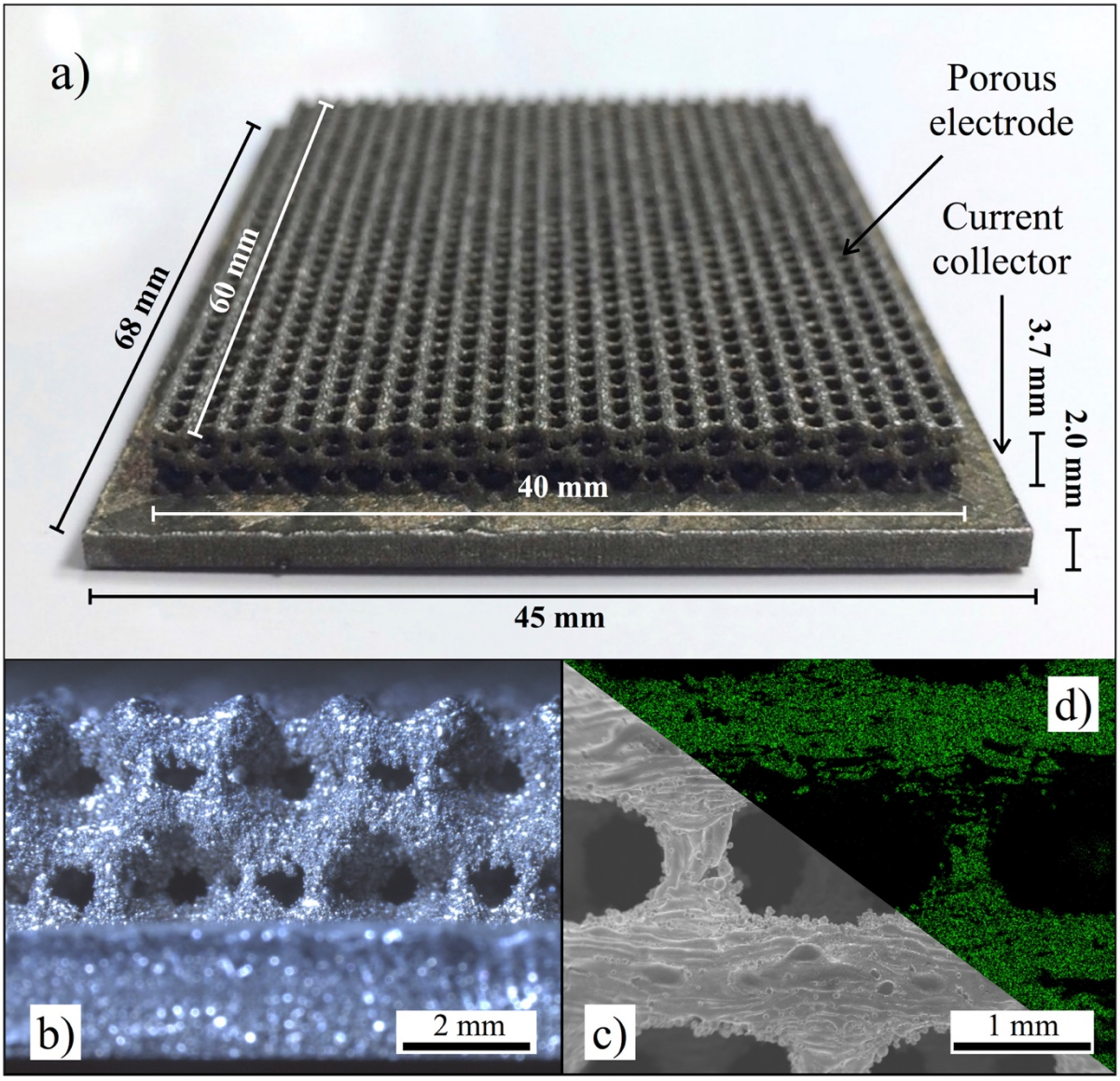
a)
Porous electrode
Current collector
68 mm
60 mm
40 mm
3.7 mm
2.0 mm
45 mm
b)
2 mm
c)
d)
1 mm

Fig. 2

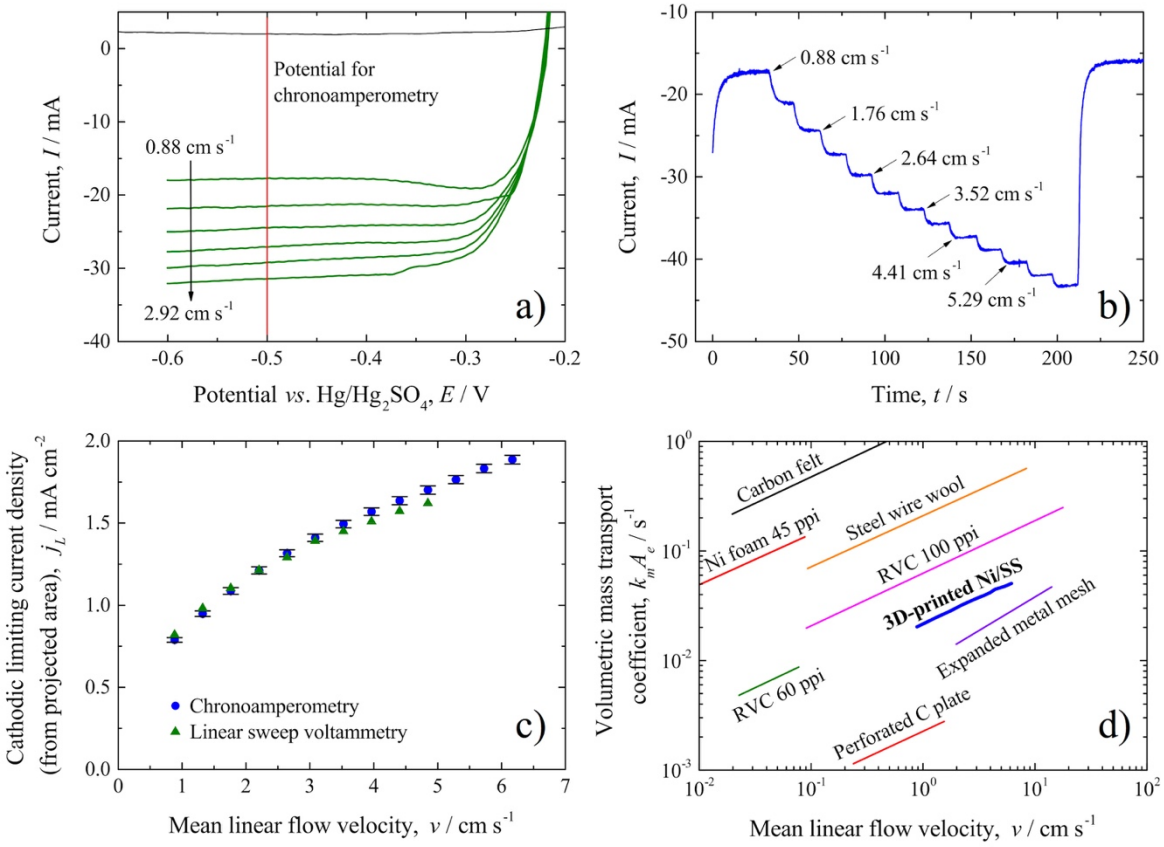
Potential for
chronoamperometry
0.88 cm s-1
2.92 cm s-1
Current, I / mA
Potential vs. Hg/Hg2SO4, E / V
a)
0.88 cm s-1
1.76 cm s-1
2.64 cm s-1
3.52 cm s-1
4.41 cm s-1
5.29 cm s-1
Current, I / mA
Time, t / s
b)
Cathodic limiting current density
(from projected area), jL / mA cm-2
Chronoamperometry
Linear sweep voltammetry
Mean linear flow velocity, v / cm s-1
c)
Volumetric mass transport
coefficient, kmAe / s-1
Carbon felt
Ni foam 45 ppi
Steel wire wool
RVC 100 ppi
3D-printed Ni/SS
Expanded metal mesh
RVC 60 ppi
Perforated C plate
Mean linear flow velocity, v / cm s-1
d)

Fig. 3